Revamping Triboelectric Output by Deep Trap Construction

Nannan Wang, ‡ Yizhe Liu, ‡ Yange Feng, Jing Yang, Yaze Wu, Boya Zhang, Yixuan Li, Bofan Li, Sheng Wang, Enyi Ye, Yong-Wei Zhang, Xian Jun Loh, Feng Zhou, Zibiao Li*, Daoai Wang**

‡ These authors contributed equally.

N. Wang, Y. Liu, Y. Feng, F. Zhou, D. Wang

State Key Laboratory of Solid Lubrication, Lanzhou Institute of Chemical Physics, Chinese Academy of Sciences, Lanzhou 730000, China. E-mail: fengyange@licp.cas.cn wangda@licp.cas.cn

Y. Liu

Center of Materials Sciences and Opto-Electronic Technology, University of Chinese Academy of Sciences, Beijing, 100049, China.

D. Wang

Qingdao Center of Resource Chemistry and New Materials, Qingdao 266100, China.

N. Wang, Bofan Li, Sheng Wang, E. Ye, X. Loh, Z. Li

Institute of Sustainability for Chemicals, Energy and Environment (ISCE2), Agency for Science, Technology and Research (A*STAR), 1 Pesek Road, Jurong Island, Singapore 627833, Republic of Singapore.

E. Ye, X. Loh, Z. Li

Institute of Materials Research and Engineering (IMRE), Agency for Science, Technology and Research (A*STAR), 2 Fusionopolis Way, Innovis #08-03, Singapore 138634, Republic of Singapore. E-mail: lizb@imre.a-star.edu.sg

Z. Li

Department of Materials Science and Engineering, National University of Singapore, 9 Engineering Drive 1, Singapore 117576, Singapore.

B. Zhang, Y. Li

State Key Laboratory of Electrical Insulation and Power Equipment, Xi’an Jiaotong University, Xi’an 710049, China

J. Yang, Y. Wu, Y. Zhang

Institute of High Performance Computing (IHPC), Agency for Science, Technology and Research (A*STAR), 1 Fusionopolis Way, #16-16 Connexis, Singapore 138632, Republic of Singapore.

Keywords: triboelectric nanogenerators, deep trap, dielectric energy storage, self-assembled molecules, internet of things

Abstract

High output performance is critical for building triboelectric nanogenerators (TENGs) for future multifunctional applications. Unfortunately, the high triboelectric charge dissipation rate has a significant negative impact on its electrical output performance. To overcome this grand challenge, we designed a new tribolayer through introducing self-assembled molecules with large energy gaps on commercial PET fibric to form carrier deep traps, which improve charge retention while decreasing dissipation rates. The deep trap density of the PET increases by two orders of magnitude, resulting in an 86% reduction in the rate of charge dissipation and a significant increase in the charge density that can be accumulated on the modified fabric during physical contact. The key explanation is that, as we stated for the first time in its mechanism, increasing the density of deep traps improves the dielectric's ability to store charges, making it more difficult for the triboelectric charges trapped by the tribolayer to escape from the deep traps, lowering the rate of charge dissipation. This TENG has a 1300% increase in output power density as a result of altering the deep trap density, demonstrating a significant improvement. This work describes a simple yet efficient method for building TENGs with ultra-high electrical output and promotes their practical implementation in the sphere of the Internet of Things.

1. Introduction

In the new era of the Internet of Things (IoT), triboelectric nanogenerators (TENGs) have been demonstrated as a low-cost, direct, and effective method to convert mechanical energy ubiquitous in natural environments into electrical energy, which can be applied in various self-powered equipment, including sensors and charging systems.[1-5] However, TENGs are limited by the rapid dissipation of interfacial charges, resulting in relatively low electrical output performance, which hinders its further applications.[6-10] Although various strategies have been reported, a tribolayer material with effective electrical storage property to minimize the adverse effects brought by charge dissipation is imperative to be developed to boost the output performance. Up till now, raising the dielectric constant of tribolayer to enhance the storage capacity of triboelectric charge has been mostly investigated to reduce charge dissipation.[11-16] However, as the dielectric constant rises, the dielectric loss also inevitably rises, which is caused by the enhanced interaction between the electric field and charges. Consequently, the electrical energy generated by friction is converted into heat energy instead of being stored or transferred, thereby reducing the effective utilization rate of electrical energy.[17-19] Additionally, the

regulation process of the dielectric constant is so complicated that it is difficult to produce it on a large scale. Therefore, to decrease triboelectric charge loss while maintaining energy conversion efficiency, novel and up scalable charge storage techniques must be developed and investigated.

Generally speaking, the charges generated during triboelectrification are stored transiently on the surface of dielectrics.[20-24] "Containers" used to store charges include chemical bonds, molecular structures or carrier traps. For the latter, two different types of traps, shallow traps and deep traps, are used to catch these charges. Among them, the charges in shallow traps that are easy to escape are preferentially dissipated to the environment, while the charges in deep traps can be stored for a long time because they are extremely difficult to escape.[25-27] As a result, the crucial factors that influence the charge dissipation rate of the tribolayer are the ability of a trap to capture charge and the capability of the trapped charge to escape from the trap. Despite the fact that the research on the mechanism of carrier trapping and de-trapping by carrier traps has promoted the development of semiconductor industry and high voltage technology,[28-31] there are limited reports on how carrier traps, especially deep traps, affect the electrical output performance of TENGs. In fact, the material's triboelectric charge density will be impacted by the density of deep traps during the contact electrification process. The dielectric material with widely distributed higher-density deep traps can store more triboelectric charges on the surface of the tribolayer, preventing their dissipation to the environment.

Herein, we investigated the impact of deep carrier trap on the charge dissipation rate and charge accumulation on the tribolayer surface of TENG from the standpoint of trap distribution. By molecular self-assembly, the (N, N-Dimethyl-3-aminopropyl) trimethoxysilane (KH556) molecule with a large energy gap was exploited to construct deep traps that located at the interface of the two molecules in polyethylene terephthalate (PET), which is supported by density functional theory calculations. The current output density of KH556@PET-based TENG dramatically increased by 530% when compared to pure PET-based TENG. Moreover, the TENG generated a 1300% enhancement in output power by successfully building the deep traps, which made it possible to power 240 LEDs and sports watches. Energy distribution of the insulators' carrier traps showed that the deep trap density of the PET composite film with KH556 modification increased by two orders of magnitude, from 1.65×10^{19} $m^{-3}J^{-1}$ to 2.53×10^{21} $m^{-3}J^{-1}$. The elevated surface charge density of KH556@PET-based TENG was primarily determined by the increased deep trap density, as the elevated density of deep traps enhanced the tribolayer's electrical storage capabilities and lowered the rate of triboelectric charges dissipation with 86%. In view of its exceptional adaptability and electrical output capability,

the designed TENG was used as a wearable wireless remote control for model car movement, and the parallel signal processing circuit design is employed to reduce crosstalk between nearby TENG units to enhance signal stability and driving performance.

2. Results and Discussion

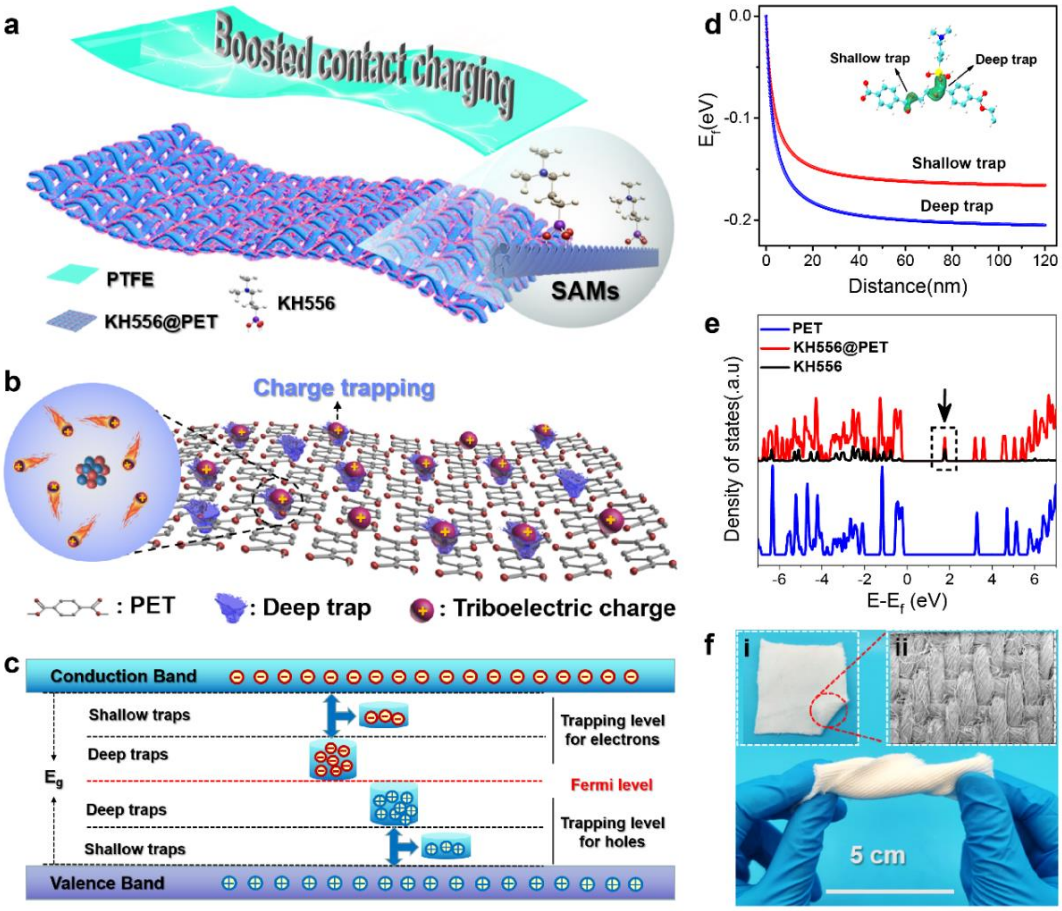

Figure 1. Strategy for building deep traps in PET fibric. (a) Schematic diagram of contact electrification between KH556@PET fabric and PTFE. **(b)** Schematic diagram of the deep traps storing charge to reduce dissipation. **(c)** Schematic representation of the distribution of shallow and deep traps in a dielectric material. **(d)** Fermi level representations at 120 nm along the thickness, for a shallow trap and a deep level. **(e)** Density of states comparison of pure PET, KH556 and KH556@PET. **(f)** Photo of KH556@PET fabric. (i) Main view and (ii) SEM photograph of KH556@PET fabric.

Benefiting from the high strength and elastic recovery ability, PET fabric is a favorable candidate for a tribolayer of flexible wearable TENGs. However, the triboelectrification capability of PET is insufficient when contact charging with PTFE due to weak polarization and excessive charge dissipation rate. In order to increase triboelectric charges stored in PET molecules to minimize charge dissipation, KH556 was introduced into PET as a deep trap

builder, as shown in **Figure 1a**. The preparation process of KH556@PET fabric is shown in **Figure S1**. When KH556 is grafted onto PET molecules, deep traps are built at their interface to catch triboelectric charges. The charges stored in the deep traps are extremely difficult to escape, which may reduce the dissipation rate and boost the contact charging ability of the modified PET. A schematic diagram is shown in Figure 1b. The energy barrier and the capture cross section of the carrier trap are responsible to confine the charge in the deep trap.[32-34] Shallow traps and deep traps are the two main categories of carrier traps. In the bandgap, shallow traps for electrons are those that are close to the conduction band (LUMO), whereas shallow traps for holes are those close to the valence band (HOMO), as illustrated in Figure 1c. Their energy levels are much closer to the band edges, which means that the energy required for a charge carrier to escape from a shallow trap is low, making it more likely that a charge carrier can escape from the trap. On the other hand, the deep traps for electrons and holes are situated away from the conduction and valence bands, respectively (middle of the bandgap). Their energy levels are significantly deep in the bandgap so that the energy required for a charge carrier to escape from a deep trap is high, making it difficult for a charge carrier to escape from the trap. Therefore, deep traps with higher charge detachment energies work better than shallow traps as charge storage carriers in the tribolayer. To clearly explain why deep traps are more suitable than shallow traps as containers for storing the triboelectric charge of TENG, the Fermi levels at various depths in the KH556@PET lattice were calculated. The case of electron traps was calculated using a periodic model. When calculating the wave function, the CP2K-2022 software[35] was used in combination with the B3LYP function[36, 37], the GTH basis set and pseudopotential [38-40] in the density functional theory (DFT) method. The periodic wave function under the finite empty orbital was obtained by DFT calculation, and then the electronic trap was determined by the natural density. The energy relationship between the distance and the trap was calculated by the conjugate gradient method. The results show that pure PET molecules predominantly feature shallow traps, with almost no presence of deep traps as shown in **Figure S2**. However, KH556@PET molecules exhibit both deep and shallow traps (Figure 1d). Moreover, deep traps have a higher Fermi level than shallow traps in different depths, which indicates that more electronic states in the material are being filled with electrons. On the basis of the Fermi level of the traps, isosurface map to visualize electron traps were drawn by VMD-1.9.3, as shown in the inset of Figures S2 and 1d. According to the findings, shallow traps were found inside PET molecules, while deep traps were found at the interface between PET and KH556 molecules. This demonstrates that shallow traps dominate the carrier traps of pure PET, but when KH556 molecules are added, deep traps can successfully be built. In

general, the molecules employed to build deep traps typically have a high energy gap, and the electronic band gap overlaps with the altered host material.[41, 42] The results of DFT calculations of the electronic structures of pure PET, KH556 and KH556@PET show that the density of states of KH556 molecule and KH556@PET have a coincident absorption peak at 1.8 eV compared with pure PET, indicating that the electron orbital of the KH556 is located in the electronic band gap of the PET macromolecule (Figure 1e). Moreover, KH556 has an energy gap of up to 5.5 eV, which enables PET to construct stable deep traps to effectively trap and bind carriers. The molecular model of KH556@PET and the calculation process is shown in **Figure S3**. The physical object and SEM photos of the KH556@PET fabric are displayed in Figures 1f (i) and 1f (ii), respectively. The morphology of the PET fabric is well conserved after modification while maintaining excellent flexibility, which are the prerequisites for the modified PET fabric to be used as the tribolayer for the preparation of flexible and wearable TENG. Furthermore, the infrared spectroscopy (IR), X-ray photoelectron spectroscopy (XPS) and Energy dispersive spectroscopy (EDS) of the KH556@PET fabric were conducted to verify that KH556 was successfully introduced into PET, as shown in **Figure S4**.

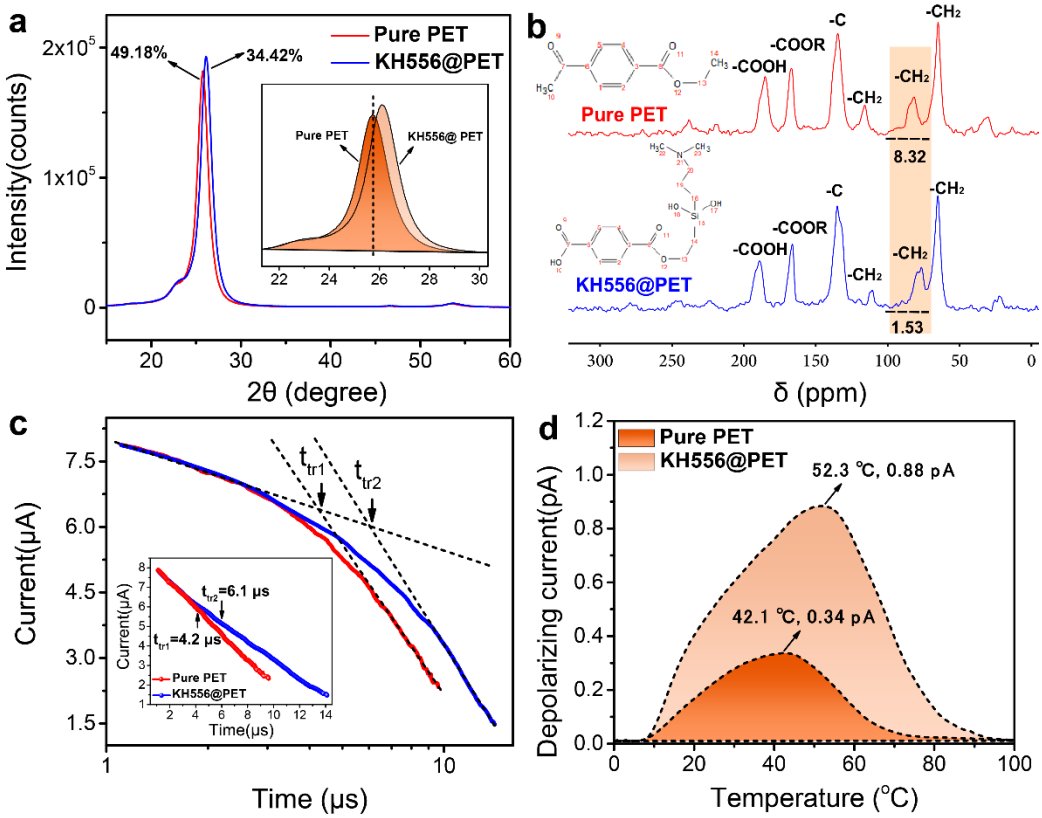

Figure 2. Characterization of deep traps in KH556@PET. (a) Comparison of XRD spectra of pure PET and KH556@PET. **(b)** ^{13}C-solid-state NMR of pure PET and KH556@PET to quantify the number of defects. **(c)** Carrier mobility in pure PET and KH556@PET measured

by time-of-flight (TOF) method. **(d)** Thermally stimulated current (TSC) curves of pure PET and KH556@PET films.

Subsequently, the defect states of KH556@PET film were characterized and quantified to verify that the deep traps were effectively constructed. **Figure 2a** shows the comparison of X-ray diffraction (XRD) spectra of pure PET and KH556@PET. Pure PET has weak and strong diffraction peaks at 22.6° and 25.7° respectively, and no strong diffraction peaks near 18°, indicating its amorphous structure.[43, 44] Furthermore, the main diffraction peak of pure PET and KH556@PET situated at 2θ=26° and a weak peak at 2θ=23° are present and correspond to the lattice plane (100) and (110), respectively.[45, 46] Then, these two diffraction peaks were deconvoluted, as shown in **Figure S5**. The results show that the two diffraction peaks of pure PET appear at 22.6° and 25.7°, while the diffraction peaks of KH556@PET appear at 22.8° and 26.1°. Compared to pure PET, the diffraction peaks of KH556@PET all shift to higher angles, which indicates that the defects of KH556@PET increase.[47-49] This is due to the fact that KH556 can create an organic film layer on the surface of PET, resulting in an increase in the amount of amorphous state on the surface of PET, decreasing the crystallinity of PET. Moreover, the development of organic thin films can prevent PET molecules from being arranged in an orderly fashion on the surface, which will also reduce PET's crystallinity. The findings from the XRD tests on pure PET and KH556@PET support our hypothesis, showing that the addition of KH556 reduces the crystallinity of PET from 49.18% to 34.42%. Thus, the main cause of the rise in defects in the modified PET composite film is the disorderly arrangement of PET molecules brought on by KH556. Next, these defects were quantified using ^{13}C-solid-state nuclear magnetic resonance (NMR), as shown in Figure 2b. Compared with the chemical shift of the methylene absorption peak of pure PET (116.8 ppm), that of KH556@PET (110.8 ppm) shifts 6 ppm lower, indicating that this is the grafting site of KH556, which is consistent with the deep trap distribution position described in the inset of Figure 1d. The difference of the normalized integral of the methylene absorption peaks of pure PET (8.32%) and KH556@PET (1.53%) was then computed in accordance with the research methodology of H. Roex et al.,[50] and the defect rate was found to be 6.79%. The results of XRD and ^{13}C-solid-state NMR prove the existence of defects in the KH556@PET composite film. These defects constitute the carrier traps in the PET film. However, to determine whether these carrier traps are deep or shallow traps, more precise characterization methods need to be used.

KH556 causes the disorganized molecular arrangement on the surface of PET, resulting in the chain disorder and dislocation in PET. This created structural flaws that serve as carrier traps, preventing carriers from moving about freely and capturing them. Based on this, carrier

mobility in pure PET and KH556@PET was measured by time-of-flight (ToF) method. Under the bias voltage 10 V, the carriers were transported in the sample and accepted by the electrode on the other side. As it is difficult to identify the location of transit time (t_{tr}) in the linear plot (Figure 2c inset), a logarithmic plot was used to identify t_{tr}. The t_{tr} value was obtained from the intersection of the linear regions[51] shown in Figure 2c. The results show that the carrier transit time in pure PET and KH556@PET films are 4.2 s and 6.1 s, respectively, indicating that the latter contains more traps that impedes carrier migration. Subsequently, more accurate characterization techniques, including thermally stimulated current (TSC) and dark conductivity, were used to verify that the traps impeding carrier movement primarily originate from deep traps. As shown in Figure 2d, the TSC testing temperature range of 0-100 ℃ covers the thermal excitation energies of the charges captured by both intrinsic traps of pure PET and KH556-introduced deep traps. The TSC spectra of pure PET and KH556@PET illustrate the two characteristic peaks of current release at 41 ℃ and 53 ℃. The thermal current comes from the release of trapped charge caused by structural defects between crystalline regions. In comparison to pure PET, the current peaks of the KH556@PET shift to a higher temperature and are increased in intensity. Structural defects produced in the incomplete crystallizing process introduce charge traps, which can be arguably identified by the increased TSC peak intensity, showing that a lot of deeper traps have been introduced by KH556. The homogeneously distributed deep traps fixed on the KH556@PET can effectively capture the injected hetero-charges and thus form intensified electrostatic shielding layers near electrodes under applied DC electric field. Consequently, the shielding layers can block charges being further injected from electrodes and impede carrier transport, so the charge dissipation in KH556@PET is remarkably suppressed. Subsequently, the trap depths and the trapped charge quantity of these two films were calculated, as shown in **Figure S6**. The trap depth of the pure PET film is estimated to be 1.7 eV, but for the KH556@PET film, the trap depth increases to 2.3 eV. Besides, the trapped charge quantity of the KH556@PET film is much higher than that of pure PET. The trapped charge quantity increases from 2.0 nC of pure PET to 4.9 nC of KH556@PET film, which proves that the KH556@PET film has a more substantial charge-capturing capability with the help of deep traps (**Table S1**). In addition, the dark conductivities of pure PET and KH556@PET were tested, as shown in **Figure S7**. The results show that pure PET has greater conductivity than KH556@PET, which further proves that the carrier traps in KH556@PET are mainly deep traps. Because shallow traps can capture more carriers to increase their concentration and improve the conductivity of the material; while deep traps restrict the movement of carriers, thereby reducing the conductivity of the material.

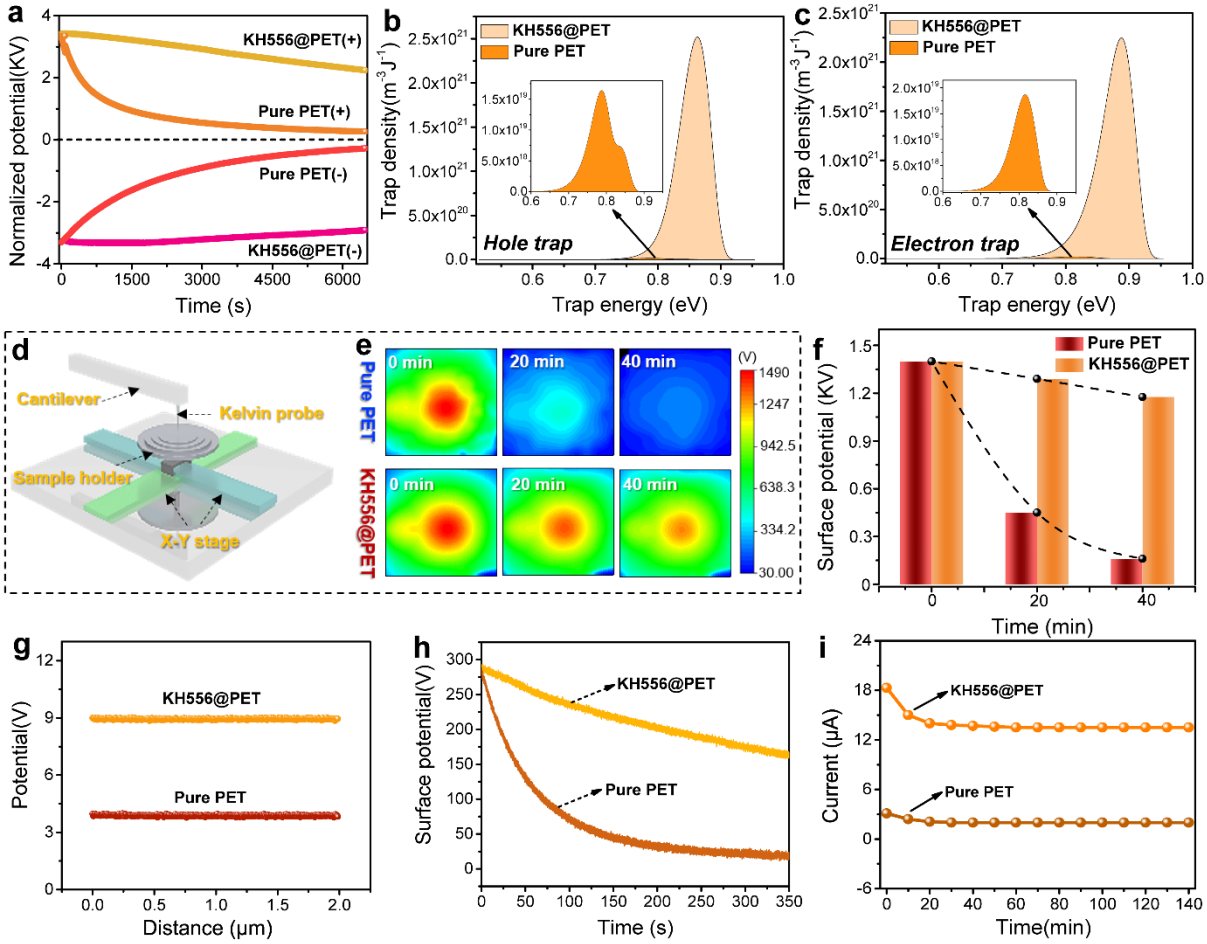

Figure 3. Triboelectric dissipation and storage properties of KH556@PET films. (a) Normalized isothermal potential decay curves of pure PET and KH556@PET films after positive (+) and negative (-) corona charging. Energy distribution of **(b)** hole traps and **(c)** electron traps of the pure PET and KH556@PET films. **(d)** Schematic illustration of the surface potential measurement on insulators after corona charging. **(e)** Surface potential decay on the pure PET and KH556@PET within 40 min. **(f)** Histogram of surface potential decay of these PET films. **(g)** Comparison of surface potential of pure PET and KH556@PET films tested by KPFM. **(h)** Real-time surface potential of pure PET and KH556@PET films. **(i)** Charge decay test of pure PET based and KH556@PET based TENGs.

After confirming that deep traps are the primary trap type in the KH556@PET film, we evaluated the density of deep traps (electron traps and hole traps) to better understand their functions in suppressing charge dissipation. The charge dissipation process heavily depends on trapping and de-trapping kinetics. An isothermal surface potential decay model is used to quantify the energy distribution of electron and hole traps in order to get insight into the surface trap states of the samples. A corona source using a "needle-grid to surface" construction first charged the sample. 12.5 kV and 3 kV dc voltage were delivered to the needle and mesh grid,

respectively. The mesh grid was positioned between the needle and the sample surface at a distance of 30 mm, allowing the sample to be charged equally to the grid potential. After being charged for 3 min, the sample was transferred in 2 s through a rotatable platform to the Kelvin probe (Trek 3455ET), where the surface potential decay curve at ambient temperature could be recorded. **Figure 3a** shows the normalized isothermal potential decay curves of pure PET and KH556@PET after positively and negatively charged. It is found that KH556@PET shows a lower charge dissipation rate regardless of positive or negative charge. Based on the theory of isothermal discharge current (IDC) proposed by Simmons[52], the density of traps $N(E_T)$ and the energy of traps E_T can be calculated by following equations:

$$N(E_T) = \frac{\varepsilon t}{q_e f_0 kT\delta L}\frac{d\varphi(t)}{dt} \quad \text{(Eq. 1)}$$

$$E_T = kTln(\gamma t) \quad \text{(Eq. 2)}$$

where ε is the permittivity of the sample and L is the thickness of the sample. δ is the penetration depth of injected electrons. q_e is the elementary charge quantity. k is the Boltzmann constant. T is the absolute temperature (303 K). γ is the escape frequency of trapped electrons, which is approximately equal to 10^{12} s^{-1}. f_0 is the rate of initial occupancy of traps. Here, we assume f_0=1 for simplification. During the isothermal potential decay process, charges in the shallow trap de-trap first, followed by charges in the deep trap. In other words, the charge release time and trap depth are connected. Therefore, it may be claimed that when shallow traps and deep traps are considered, two distinct types of decay processes occur simultaneously. In this work, the double exponential decay equation is utilized to fit the decay curves:

$$\varphi(t) = a_1\, e^{-b_1 t} + a_2 e^{-b_2 t} \quad \text{(Eq. 3)}$$

Finally, software was created to determine the trap distribution using Equation (10). As shown in Figure 3b, the hole deep trap depth of pure PET and KH556@PET are 0.79 eV and 0.86 eV, respectively. For pure PET, the deep trap density is 1.65×10^{19} $m^{-3}J^{-1}$. However, the deep trap density of in the KH556@PET film is boosted to 2.53×10^{21} $m^{-3}J^{-1}$, which increases by two orders of magnitude. Furthermore, compared with the pure PET film, the electron deep trap density of the KH556@PET film increases from 1.88×10^{19} $m^{-3}J^{-1}$ to 2.26×10^{21} $m^{-3}J^{-1}$, which also increases by two orders of magnitude (Figure 3c). The increase of deep trap density indicates that the KH556@PET film can capture more triboelectric charges during contact electrification process. More importantly, the increase in deep trap density can reduce the dissipation rate of triboelectric charges into the environment, allowing more charges to be stored by the dielectric layer. This is primarily why the introduction of KH556 to the PET film can boost the surface triboelectric charge density.

In order to intuitively demonstrate the inhibitory effect of deep traps on charge dissipation, charges were injected onto the insulator surface by a positively biased corona source, and the spatial-temporal development of the surface potential distributions was then monitored, as shown in Figure 3d. The results indicate that pure PET and KH556@PET films have almost the same initial charge (Figure 3e), but KH556@PET film has more uniform charge distribution. Moreover, the charged regions of the pure PET film dissipate rapidly within the first 20 min, reducing the local peak to 32% of the initial value. After 40 min, its surface potential decays by 89%. This is in sharp contrast to KH556@PET, whose surface potential has only decayed by 16% even after 40 min. In order to clearly show the charge dissipation rates of the two films, histogram of surface potential decay was plotted, as shown in Figure 3f. In addition to the polarized charge, we further investigated the effect of the introduction of KH556 on the dissipation rate of the triboelectric charge. First, the triboelectric charge dissipation behavior was tested at the microscopic level. After rubbing with the probe of KPFM, the surface potentials of pure PET and KH556@PET films were tested respectively, as shown in Figures 3g and **S8**. The results show that KH556@PET has a larger surface potential than pure PET. Then, the comparison of the dissipation of triboelectric charge between the two was tested at the macroscopic level. Prior to the test, the surface charge density was increased until it reached a saturated condition by colliding pure PET and KH556@PET films with PTFE films using a motor. The surface potential is then promptly captured by the surface potential meter, as shown in Figure 3h. The findings demonstrate that the surface potential of the KH556@PET film decreases at a slower rate than that of the pure PET film. Additionally, Figure 3i shows the charge decay test of pure PET-based and KH556@PET-based TENGs. The structure and working mechanism of TENG are shown in **Figure S9**. To measure the decay performance, the TENG operation process was stopped when it reached the stable and maximum short-circuit current (I_{sc}) value. The TENG was then driven for one cycle to acquire the initial I_{sc1} value and stopped once more for 10 min prior to testing the subsequent I_{sc2} value. To avoid obvious charge accumulation, there was no continuous friction applied to the tribo-electrodes during this operation. The entire process took 140 min in order to collect a series of I_{sc} readings. The results indicate that over the course of 140 min, the electrical output of the pure PET-based TENG experienced a 33.3% decrease, whereas the KH556@PET-based TENG exhibited a more modest decline of 26.2%. It suggests that, in comparison to pure PET, the KH556@PET demonstrates better charge storage capability.

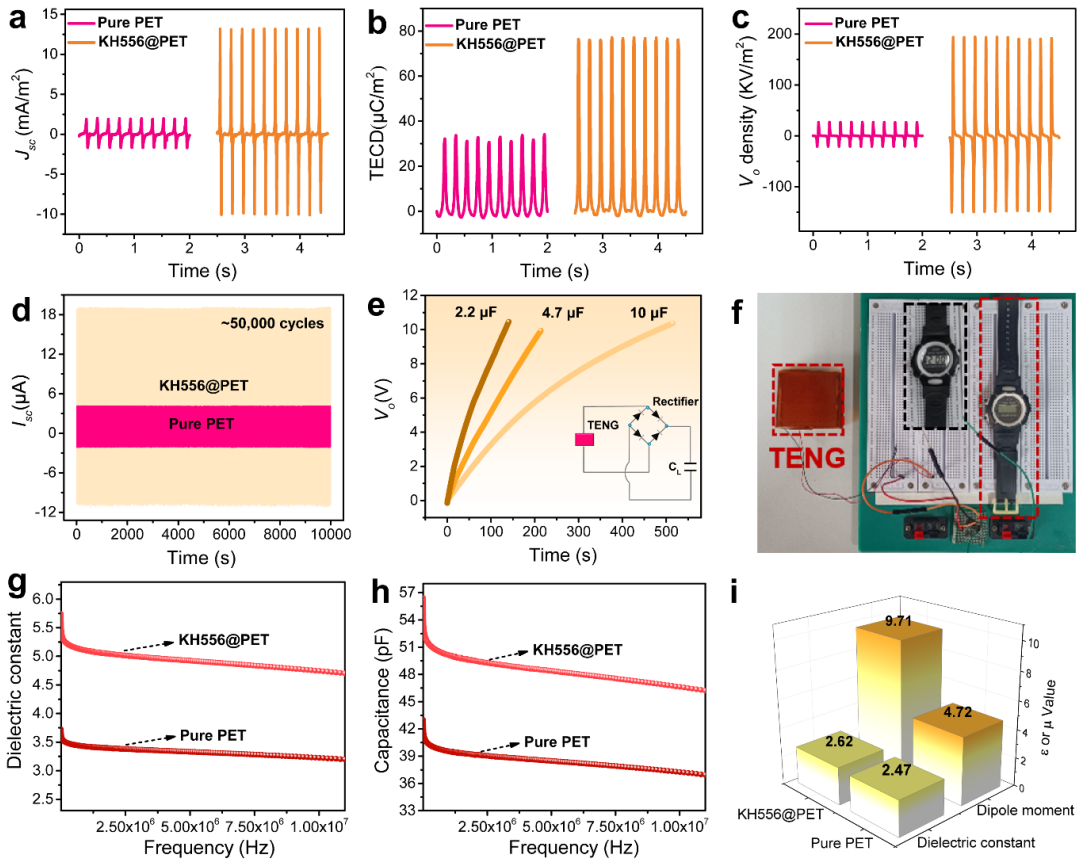

Figure 4. Electrical output performance of KH556@PET-based TENG. Comparison of **(a)** current density (J_{sc}), **(b)** triboelectric charge density (TECD) and **(c)** output voltage (V_o) density for pure PET based and KH556@PET based TENGs. **(d)** Comparison of I_{sc} stability of these two TENGs within 50,000 cycles. **(e)** Curves and circuit diagram of KH556@PET based TENG charging capacitors. **(f)** Photo of demonstration experiment of KH556@PET based TENG powering sports watch. Comparison of **(g)** dielectric constant and **(h)** capacitance of pure PET and KH556@PET films. **(i)** Comparison of dielectric constant and dipole moment calculated by DFT of pure PET and KH556@PET.

The reduction of the charge dissipation rate of the tribolayer is the key factor to achieve an ultrahigh electrical output of TENG. In order to verify the improvement of electrical output, the current density of pure PET-based and KH556@PET-based TENGs were tested, as shown in **Figure 4a**. The results show that compared with pure PET-based TENG, the current density (J_{sc}) of KH556@PET-based TENG increases by 530% from 2.1 mA/m^2 to 13.3 mA/m^2, showing a huge boost in electrical output. Furthermore, the triboelectric charge density obtained by I_{sc} integration increases by 132% from 33.4 μC/m^2 to 77.6 μC/m^2 (Figure 4b). The V_o density of KH556@PET-based TENG rises from 30 KV/m^2 to 197 KV/m^2 at a rate of 560% when compared to pure PET-based TENG (Figure 4c), which is compatible with the change result of current density. The thickness of the triboelectric layer plays a pivotal role in determining the

optimal triboelectric performance. Variations in thickness can lead to charge recombination and impact electrostatic induction.[53, 54] The effect of tribolayer thickness on the electrical output of the TENG was tested, as shown in **Figure S10**. Out of all the thickness variations, the TENG using 75 μm PET, following the molecular assembly, exhibited the highest current density and voltage density. Then, a stability test was conducted, and the results are given in Figure 4d, in order to guarantee the KH556@PET-based TENG's consistent and steady output under real-life circumstances. The I_{sc} of the KH556@PET-based TENG is constant at roughly 21.3 μA after more than 50,000 cycles, showing that KH556@PET-based TENG can be utilized steadily as an energy collecting device for a long period. Subsequently, the works in recent years to increase the electrical output by chemically modifying the tribolayer of TENG to increase the dielectric constant were summarized, as shown in **Table S2**. In general, a TENG with a friction layer featuring a high dielectric constant tends to yield a larger electrical output. Nevertheless, KH556@PET boasts a dielectric constant of merely 5.2. Surprisingly, it exhibits a superior electrical output, with a current output, compared to TENGs that are typically chemically modified to augment their dielectric constants. This emphasizes that the generation of deep traps can significantly enhance the electrical output of TENGs, and this enhancement is achieved not solely through an increase in dielectric constant. The charge amounts of pure PET and KH556@PET and the power density comparison of the two TENGs are shown in **Figures S11a** and 11b. Compared with the pure PET-based TENG, the power density of the KH556@PET-based TENG increased from 75 mw/m^2 to 1050 mw/m^2, an increase of 1300%. To demonstrate that the KH556@PET-based TENG can successfully power the electrical appliances, the curves for it to charge three capacitors with different capacities were collected, as displayed in Figure 4e. The findings demonstrate that this TENG can charge capacitors of 2.2 μF, 4.7 μF, and 10 μF to 10 V accordingly in 139 s, 214 s and 517 s. The circuit diagram of TENG charging the capacitor is shown in the inset in Figure 4e, and the role of the rectifier is to convert the alternating current generated by the TENG into direct current. As illustrated in the digital photographs in Figures 4f, S11c and **Video S1**, driven by hand flapping, the KH556@PET-based TENG can easily light up 240 LEDs and a sport watch, demonstrating this TENG's excellent energy-harvesting performance.

In addition to the impact of deep traps on the electrical output of TENG, the mechanism of secondary factors has been explored, such as electronic effects and dielectric constants. First, the change in the dielectric constant of the PET film by KH556 modification was explored, as shown in Figure 4g. For the pure PET film, the initial dielectric constant is measured to be approximately 3.7 in the frequency of 40 Hz. The dielectric constant significantly decreases to

about 3.3 in the higher frequency band (10^6 to 10^7 Hz). This is due to the polymers' inability to keep up with the fluctuating external field during dipole relaxation. With the introduction of the KH556, the dielectric constant obvious improved. The KH556@PET shows a dielectric constant value of 5.7 at a frequency of 40 Hz. When the frequency is increased to 10^6 - 10^7 Hz, the dielectric constant is stable at 4.8. The capacitances of pure PET and KH556@PET reveal the same pattern, with KH556 increasing PET capacitance by 24% at 10^6-10^7 Hz (Figure 4h). Furthermore, there is no significant change in the loss tangent of all samples, as shown in **Figure S12a**, which means that the dielectric constant values are quite reliable.[55] Subsequently, DFT was used to calculate the changes in the dielectric constant and dipole moment of PET due to the introduction of KH556, as shown in Figure 4i and **Table S3**. The selection of comparative samples and calculation process is shown in Figures S12b. Additionally, the electron-donating effect of tertiary amino groups on the electrical output of TENG was calculated using DFT, as shown in **Figures S13** and **S14**. The findings demonstrate that, similar to the effect of the dielectric constant on the electrical output of TENG, the electronic effect of tertiary amino groups does not significantly affect the electrical output of TENG either, indicating that the increase in electrical output of TENG is primarily attributed to the deep trap density-induced decrease in triboelectric charge dissipation.

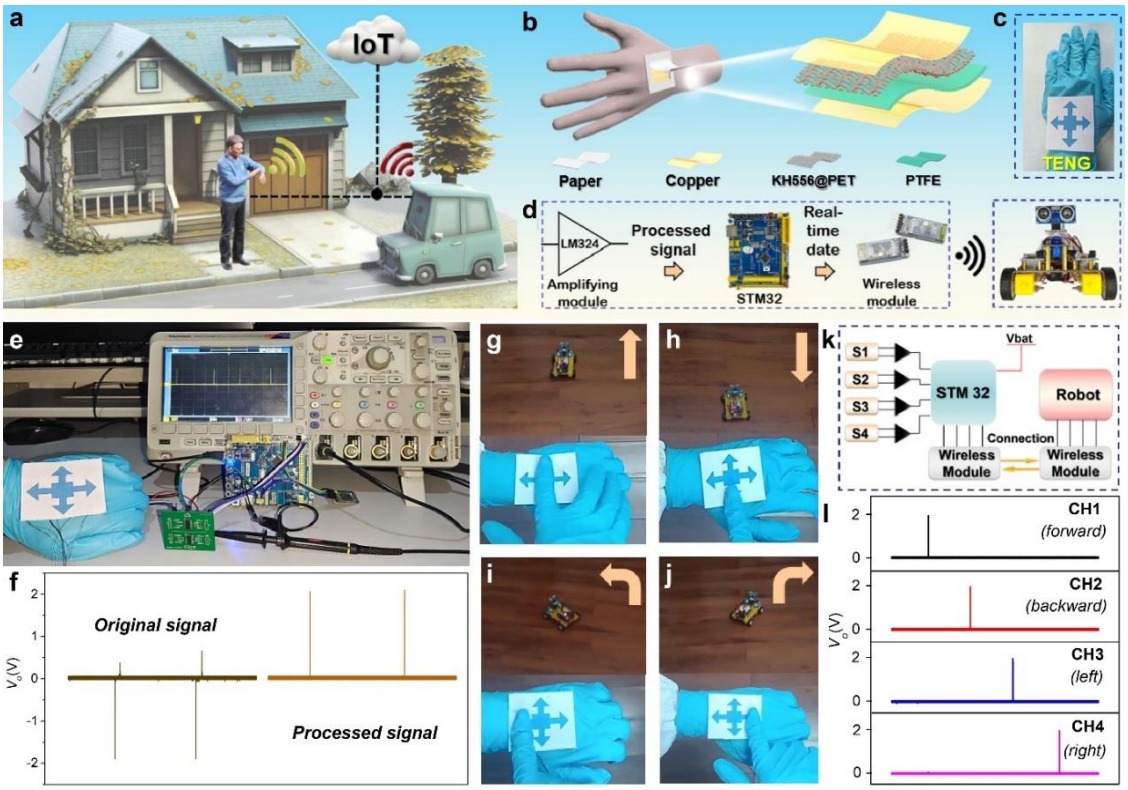

Figure 5. Application of KH556@PET based TENG in IoT. **(a)** Schematic diagram of the application of KH556@PET-based TENG in wearable electronic remote control. **(b)** Schematic

diagram and **(c)** optical image of KH556@PET fabric-based TENG structure attached to the back of the hand. **(d)** Photo of the custom IoT module consisting of a signal processing circuit, a wireless transmission module, a microcontroller unit (MCU) with an embedded analog-to-digital (ADC) converter. **(e)** The optical photo of the signal generated by TENG processed by the IoT module. **(f)** The original *Vo* signal and *Vo* processed signal of KH556@PET-based TENG. Optical images of illustrating the controlling process and the optical images of the remote-control car, where finger tapping on different positions corresponds to **(g)** "forward", **(h)** "backward", **(i)** "left", and **(j)** "right". **(k)** Circuit diagram of the control panel. **(l)** The processed signal of the KH556@PET fabric-based TENG recorded when controlling the model car.

Due to the ultrahigh electrical output performance, the KH556@PET-based TENG can be applied to energy harvesting in the environment to power small electronic devices. Moreover, in view of the excellent wash resistance (**Figure S15**) of KH556@PET fabric, this TENG can be used as a power module for wearable electronic devices in the Internet of Things. Schematic diagram of the KH556@PET-based TENG applications in wearable electronic remote control is shown in **Figure 5a**. The electrical signal generated by the integrated wearable TENG attached to the back of the hand is processed by a IoT module that sends instructions to the terminal to control the movement of a car. As shown in Figure 5b, TENG unit was made of KH556@PET fabric/Cu and PTFE/Cu as electrodes and PDMS as supports. The integrated device was encapsulated by a patterned paper. To demonstrate the ability of the TENG device to drive a robot, we integrated the device into a "2*2" array sensor network, where the 4 units represent front, back, left, and right, as shown in Figure 5c. The customized IoT module was composed of signal processing circuits, a wireless transmission module, a microcontroller unit (MCU) with embedded analog-to-digital (ADC) converters (Figure 5d). The 4 TENG units were assembled with the electrical wires connected to the customized IoT module fixed on the rear area of the hand as illustrated in Figure 5e. The customized IoT modules were configured to ensure that the final analog output of each TENG units were finely resolved while staying within the input voltage range of the ADC. The customized IoT module received the pulse signal from the TENG unit, and through the signal processing circuit, reversely amplified the original signal of the TENG unit into a pulse signal of 0-3.3V (Figure 5f). Conditioned signals were acquired by ADC module of MCU and converted into control signal to remotely control the robot to step forward, backward, turn left or turn right, as shown in Figures 5g-5j and **Video S2**. The circuit diagram of the IoT module is shown in Figure 5k. Since the TENG unit is a high-resistance element, crosstalk from the adjacent TENG units remains a great challenge for

controlling arrays. In this work, we have designed four parallel signal processing circuits which can greatly eliminate crosstalk from the adjacent TENG units and improve the stability and driving ability of the signal. As shown in Figure 5l, the pulse control signals generated by the 4 channels have no crosstalk, so that the stable control of the robot by TENG can be achieved.

3. Conclusion

In summary, by manipulation of the trap distribution in the tribolayer, we propose a new strategy to suppress triboelectric charge dissipation to boost the electric output of TENGs. Benefiting from the high energy gap of KH556, the introduction of KH556 into PET can establish stable and uniformly distributed deep traps at the molecular interface. The deep traps can effectively trap the triboelectric charge, making it difficult to escape, which significantly increases the triboelectric charge density of the tribolayer. Experimental results show that the deep trap density of the modified PET is two orders of magnitude higher than that of pure PET, which enhances the ability of the modified PET to store triboelectric charges and slows the dissipation of triboelectric charges by 86%. As a result, the current density and voltage density of KH556@PET-based TENG are enhanced by 530% and 577%, respectively, when compared with pure PET-based TENG. The KH556@PET-based TENG can generate a maximum output signal of 13.3 mA/m^2 and 197 KV/m^2 to power 240 LEDs or a sport watch and it is demonstrated to control the motion of a model car. This study promotes the use of TENGs in practical IoT applications by outlining a quick and efficient way to construct TENGs with great performance.

Supporting Information

Supporting Information is available from the Wiley Online Library or from the author.

Acknowledgements

The authors would like to thank the financial support of the Program for Taishan Scholars of Shandong Province (No. ts20190965), the National Natural Science Foundation of China (No. U21A2046, 52205230, 52205233, 522752195), the Key Research Program of the Chinese Academy of Sciences (Grant No. ZDBS-ZRKJZ-TLC010), the Western Light Project of CAS (xbzg-zdsys-202118), Major Science and Technology Projects in Gansu Province (No. 22ZD6GA002) and the Major Program of the Lanzhou Institute of Chemical Physics, CAS (No. ZYFZFX-5). N. Wang and Z. Li would also like to thank the financial support from the Agency for Science, Technology and Research (A*STAR), Science and Engineering Research Council (SERC) Central Research Fund (Use-inspired Basic Research) for this work.

Conflicts of interest

The authors declare no conflict of interest.

References

[1] M. Li, H. Lu, S. Wang, R. Li, J. Chen, W. Chuang, F. Yang, Y. Lin, C. Chen, Y. Lai, *Nat. Commun.* **2022**, 13, 938.

[2] L. Zhang, H. Cai, L. Xu, L. Ji, D. Wang, Y. Zheng, Y. Feng, X. Sui, Y. Guo, W. Guo, *Matter* **2022**, 5, 1532.

[3] Z. L. Wang, *Adv. Energy Mater.* **2020**, 10, 2000137.

[4] J. Luo, W. Gao, Z. L. Wang, *Adv. mater.* **2021**, 33, 2004178.

[5] C. Wu, A. C. Wang, W. Ding, H. Guo, Z. L. Wang, *Adv. Energy Mater.* **2019**, 9, 1802906.

[6] J. Zhong, X. Hou, J. He, F. Xue, Y. Yang, L. Chen, J. Yu, J. Mu, W. Geng, X. Chou, *Nano Energy* **2022**, 98, 107289.

[7] W. He, C. Shan, H. Wu, S. Fu, Q. Li, G. Li, X. Zhang, Y. Du, J. Wang, X. Wang, *Adv. Energy Mater.* **2022**, 12, 2201454.

[8] N. Wang, Y. Liu, E. Ye, Z. Li, D. Wang, *Mater. Res. Lett.* **2022**, 10, 97.

[9] W. He, C. Shan, S. Fu, H. Wu, J. Wang, Q. Mu, G. Li, C. Hu, *Adv. Mater.* **2023**, 35, 2209657.

[10] Y. Xie, Q. Ma, B. Yue, X. Chen, Y. Jin, H. Qi, Y. Hu, W. Yu, X. Dong, H. Jiang, *Chem. Eng. J.* **2023**, 452, 139393.

[11] B. Fan, G. Liu, X. Fu, Z. Wang, Z. Zhang, C. Zhang, *Chem. Eng. J.* **2022**, 446, 137263.

[12] N. Wang, D. Yang, W. Zhang, M. Feng, Z. Li, E. Ye, X. J. Loh, D. Wang, *ACS Appl. Mater. Interfaces* **2022**, 15, 997.

[13] S. K. Ghosh, J. Kim, M. P. Kim, S. Na, J. Cho, J. J. Kim, H. Ko, *ACS nano* **2022**, 16, 11415.

[14] Z. Zheng, J. Xia, B. Wang, Y. Guo, *Nano Energy* **2022**, 95, 107047.

[15] H. Park, S. J. Oh, D. Kim, M. Kim, C. Lee, H. Joo, I. Woo, J. W. Bae, J. H. Lee, *Adv. Sci.* **2022**, 9, 2201070.

[16] X. Wu, X. Chen, Q. Zhang, D. Q. Tan, *Energy Storage Mater.* **2022**, 44, 29.

[17] W. Tong, Y. Zhang, Q. Zhang, X. Luan, Y. Duan, S. Pan, F. Lv, Q. An, *Carbon* **2015**, 94, 590.

[18] C. Yang, Y. Lin, C. Nan, *Carbon* **2009**, 47, 1096.

[19] C. F. Tseng, C. H. Hsu, *J. Am. Ceram. Soc.* **2009**, 92, 1149.

[20] H. Wang, H. Sakamoto, H. Asai, J. Zhang, T. Meboso, Y. Uchiyama, E. Kobayashi, E. Takamura, S. Suye, *Nano Energy* **2021**, 90, 106515.

[21] N. Cui, L. Gu, Y. Lei, J. Liu, Y. Qin, X. Ma, Y. Hao, Z. L. Wang, *ACS nano* **2016**, 10, 6131.

[22] Y. Zi, J. Wang, S. Wang, S. Li, Z. Wen, H. Guo, Z. L. Wang, *Nat. commun.* **2016**, 7, 10987.

[23] W. Yan, Y. Liu, P. Chen, L. N. Cao, J. An, T. Jiang, W. Tang, B. Chen, Z. L. Wang, *Adv. Energy Mater.* **2022**, 12, 2103677.

[24] A. Ahmed, I. Hassan, M. F. El-Kady, A. Radhi, C. K. Jeong, P. R. Selvaganapathy, J. Zu, S. Ren, Q. Wang, R. B. Kaner, *Adv. Sci.* **2019**, 6, 1802230.

[25] Z. Zhou, J. Liu, R. Long, L. Li, L. Guo, O. V. Prezhdo, *J. Am. Ceram. Soc.* **2017**, 139, 6707.

[26] C. Qin, T. Matsushima, T. Fujihara, W. J. Potscavage Jr, C. Adachi, *Adv. Mater.* **2016**, 28, 466.

[27] M. Righetto, S. S. Lim, D. Giovanni, J. W. M. Lim, Q. Zhang, S. Ramesh, Y. K. E. Tay, T. C. Sum, *Nat. commun.* **2020**, 11, 2712.

[28] C. Wild, M. Huettel, A. Klueter, S. G. Kremb, M. Y. Rasheed, B. B. Jørgensen, *Nature* **2004**, 428, 66.

[29] G. Kim, H. Min, K. S. Lee, D. Y. Lee, S. M. Yoon, S. I. Seok, *Science* **2020**, 370, 108.

[30] T. A. Doherty, A. J. Winchester, S. Macpherson, D. N. Johnstone, V. Pareek, E. M. Tennyson, S. Kosar, F. U. Kosasih, M. Anaya, M. Abdi-Jalebi, *Nature* **2020**, 580, 360.

[31] Z. Yang, X. Wang, Y. Chen, Z. Zheng, Z. Chen, W. Xu, W. Liu, Y. Yang, J. Zhao, T. Chen, *Nat. Commun.* **2019**, 10, 4540.

[32] Y. Wang, K. Cheung, *Appl. Phys. Lett.* **2007**, 91, 113509.

[33] J. Li, Z. Yuan, S. Chen, X. Gong, S. Wei, *Chem. Mater.* **2019**, 31, 826.

[34] S. W. Johnston, R. S. Crandall, A. Yelon, *Appl. Phys. Lett.* **2003**, 83, 908.

[35] K.-i. Ataka, T. Yotsuyanagi, M. Osawa, *J. Phys. Chem.* **1996**, 100, 10664.

[36] T. Yanai, D. P. Tew, N. C. Handy, *Chem. Phys. Lett.* **2004**, 393, 51.

[37] W. Kohn, L. J. Sham, *Phys. Rev.* **1965**, 140, A1133.

[38] W. Liu, Y. R. Shen, *Proc. Natl. Acad. Sci.* **2014**, 111, 1293.

[39] Z. D. Schultz, S. K. Shaw, A. A. Gewirth, *J. Am. Chem. Soc.* **2005**, 127, 15916.

[40] J. F. Li, Y. F. Huang, Y. Ding, Z. L. Yang, S. B. Li, X. S. Zhou, F. R. Fan, W. Zhang, Z. Y. Zhou, D. Y. Wu, *Nature* **2010**, 464, 392.

[41] X. D. Zhao, W. F. Sun, H. Zhao, *Polymers* **2019**, 11, 592.

[42] Y. Zhou, J. Yang, H. Zhao, W. Sun, M. Gao, X. Zhao, M. Hu, S. Xie, *Materials* **2019**, 12, 1094.

[43] B. Demirel, A. Yaraş, H. Elcicek, *BAÜ Fen Bil. Enst. Dergisi Cilt* **2011**, 13, 26.

[44] N. Murthy, C. Bednarczyk, P. Rim, C. Nelson, *J. Appl. Polym. Sci.* **1997**, 64, 1363.

[45] V. Kumar, Y. Ali, R. Sonkawade, A. Dhaliwal, *Nuclear Instruments and Methods in Physics Research Section B: Beam Interactions with Materials and Atoms* **2012**, 287, 10.

[46] K. Chikaoui, M. Izerrouken, M. Djebara, M. *Radiat. Phys. Chem.* **2017**, 130, 431.

[47] P. Saini, R. Sharma, N. Chadha, *Indian J. Pure Appl. Phys.* **2017**, 55, 625.

[48] M. Strankowski, D. Włodarczyk, Ł. Piszczyk, J. Strankowska, *J. Spectrosc.* **2016**,1.

[49] J. Chen, J. Graetz, *ACS Appl. Mater. Interfaces* **2011**, 3, 1380.

[50] H. Roex, P. Adriaensens, D. Vanderzande, J. Gelan, *Macromolecules* **2003**, 36, 5613.

[51] L. Mohan, S. R. Ratnasingham, J. Panidi, M. Daboczi, J. S. Kim, T. D. Anthopoulos, J. Briscoe, M. A. McLachlan, T. Kreouzis, *ACS Appl. Mater. Interfaces* **2021**, 13, 38499.

[52] B. Zhang, Q. Wang, Y. Zhang, W. Gao, Y. Hou, G. Zhang, *Nanoscale* **2019**, 11, 18046.

[53] D. W. Kim, J. H. Lee, I. You, J. K. Kim, U. Jeong, *Nano Energy* **2018**, 50, 192.

[54] M. P. Kim, C. W. Ahn, Y. Lee, K. Kim, J. Park, H. Ko, *Nano Energy* **2021**, 82, 105697.

[55] J. W. Lee, H. J. Cho, J. Chun, K. N. Kim, S. Kim, C. W. Ahn, I. W. Kim, J. Kim, S. Kim, C. Yang, *Sci. adv.* **2017**, 3, e1602902.

Table of Contents

A flexible TENG with ultrahigh electrical output for application in IoT is developed by constructing deep traps from the incorporation of KH556. The deep traps can effectively trap triboelectric charges and reduce the rate of charge dissipation, resulting in a 1300% enhancement in output power density.

Nannan Wang, ‡ Yizhe Liu, ‡ Jing Yang, Yaze Wu, Boya Zhang, Yixuan Li, Bofan Li, Sheng Wang, Enyi Ye, Yong-Wei Zhang, Xian Jun Loh, Feng Zhou, Zibiao Li, Daoai Wang**

Revamping Triboelectric Output by Deep Trap Construction

ToC figure

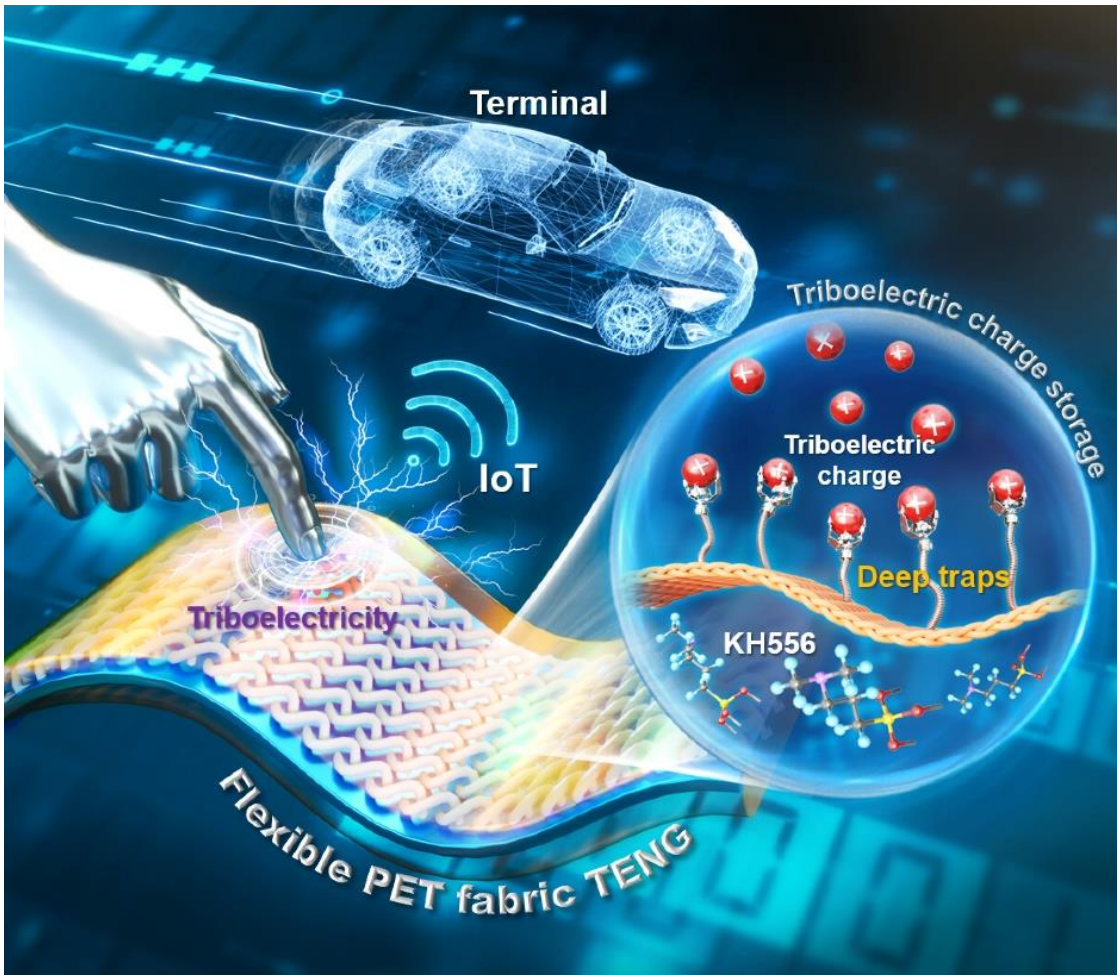
Terminal
IoT
Triboelectricity
Flexible PET fabric TENG
Triboelectric charge storage
Triboelectric charge
Deep traps
KH556